PCCP

PAPER

View Article Online
View Journal | View Issue

Cite this: *Phys. Chem. Chem. Phys.*, 2015, **17**, 29723

Interfacial band alignment for photocatalytic charge separation in TiO_2 nanotube arrays coated with CuPt nanoparticles†

Samira Farsinezhad,‡[a] Himani Sharma‡[a] and Karthik Shankar*[ab]

Received 22nd September 2015,
Accepted 14th October 2015

DOI: 10.1039/c5cp05679a

www.rsc.org/pccp

n-Type anatase-phase one-dimensional TiO_2 nanostructure arrays coated with nanoparticles of Cu or CuPt have emerged as high performance photocatalysts for both photooxidation and photoreduction. The properties of the catalyst-promoter interface are recognized to be critical to this high performance but are largely unknown. Using X-ray and ultraviolet photoelectron spectroscopies (XPS/UPS), we probed the electronic properties of the CuPt–TiO_2 interface in transparent TiO_2 nanotube arrays (TTNTAs) coated with photodeposited CuPt nanoparticles (CuPt–TTNTA hybrids) as well as those coated with sputtered CuPt (Sput-CuPt–TTNTA hybrids). XPS and UPS spectra provided the evidence of a Schottky barrier with a band-bending of 0.49–0.67 eV at the CuPt–TiO_2 interface in CuPt–TTNTA hybrids due to which photo-excited electrons are expected to be retained in the TiO_2 while photoexcited holes will be collected by the CuPt nanoparticles. For Sput-CuPt–TTNTA hybrids, no such band-bending was observed. These results point to the importance of the metal nanoparticle preparation technique on interfacial band-alignments and challenge the conventional understanding of the promoting action of noble metal nanoparticles on TiO_2 photocatalysts as sinks for photoexcited electrons.

The n-type semiconducting anatase phase of titanium dioxide (TiO_2) is one of the most potent semiconductors for photocatalytic and photoelectrochemical device applications owing to its various advantageous properties such as the strong oxidizing power of photogenerated holes, nontoxicity, high resistance to photocorrosion, high chemical stability and low cost.[1] Most photocatalytic reactions are multi-step electron transfer reactions due to which electron–hole pair recombination losses, activation barriers at each step and back-reactions of intermediate products can have a catastrophic effect on overall reaction yields.[2–5] Furthermore, because of the way in which photocatalysts are deployed, an external bias to drive the separation of charge carriers is not present. In this context, nanostructuring the TiO_2 is highly effective for improving the photocatalytic action because of the resulting high surface-to-volume ratio and the proximity of carrier photogeneration to carrier utilization. A high surface area increases the availability of reaction sites and enables a greater amount of co-catalyst/promoter loading to reduce activation barriers while the small particle size ensures that the distance from the site of carrier photogeneration to the site of the chemical reaction is comparable to the minority carrier retrieval length (diffusion length + width of the depletion region, if present).

Although zero-dimensional TiO_2 structures such as nanoparticles (NPs) and nanoshells benefit similarly from the advantages of nanostructuring outlined above and have been studied for a much longer duration both in isolation and with suitable noble metal co-catalysts, one-dimensional (1-D) TiO_2 structures such as nanorods (NRs) and nanotubes (NTs) loaded with suitable co-catalysts currently outperform TiO_2 nanoparticles and nanoparticulate films as photocatalysts for CO_2 photoreduction.[6,7] There are several differences between the structure(s) and properties of TiO_2 NPs and those of NTs/NRs (with smallest dimension comparable to the NP diameter). In nanorods and nanotubes, individual grains are elongated along the NR/NT axis while their width is determined by the lateral dimension (diameter or wall-thickness) of the NRs/NTs. The anisotropy induced by the resulting high aspect ratios in the range 15–40 changes the interactions of charge carriers and the crystallographic texture of NT/NR surfaces due to which band densities of states, surface energies, work-functions and trap distributions are significantly different than in nanoparticles.[8–11] Indeed, the dynamics of carrier

[a] *Department of Electrical and Computer Engineering, University of Alberta, 9107 - 116 St, Edmonton, Alberta, Canada T6G2 V4. E-mail: kshankar@ualberta.ca*
[b] *NRC National Institute for Nanotechnology, 11421 Saskatchewan Dr NW, Edmonton, Canada AB T6G 2M9*

† Electronic supplementary information (ESI) available: Experimental details and supplementary figures relating to the electronic band-structure, nanotube morphology, photoemission spectra and depletion region formation. See DOI: 10.1039/c5cp05679a

‡ Both authors contributed equally to this study.

recombination in TiO_2 nanotubes and nanorod arrays have been found to be significantly different from nanoparticles of comparable size.[12–16] The interactions of light with spherical and rod-type structures are different owing to the scattering of nanoparticles governed by the exact solutions given by Mie theory[17] and that of nanorods/nanotubes affected by optical anisotropy and approximately described by Gans theory.[18] While the co-catalysts in nanoparticulate photocatalysts are also nanoparticles of roughly the same size and present a single length scale, co-catalyst NPs are much smaller than the length of NRs/NTs resulting in multiple length scales, a desirable feature for high performance photocatalysis.[19]

When 1-D anatase-phase TiO_2 nanostructures are combined with a suitable co-catalyst, efficient photocatalytic activity results. Au and Pt nanoparticles formed on TiO_2 nanotubes by sputtering followed by thermal dewetting and dealloying showed a remarkable increase in efficiency for photocatalytic water splitting in comparison to TiO_2 nanoparticles.[20,21] The highest reported values of CO_2 photoreduction ($\sim$0.5 μmol cm^{-2} h^{-1}) for broadband illumination in the scientific literature for any catalyst have been obtained using 1-D TiO_2 loaded with a nano-sized platinum-containing co-catalyst.[22–27] Yet, the exact electronic band-alignment at the Pt–TiO_2 interface is unknown. The Bardeen model for Fermi level pinning involving metal-induced gap states is known to be less relevant to large bandgap oxides.[28] The Shockley-Anderson model[29] for band-alignment at a semiconductor heterojunction suggests the formation of a Schottky barrier between TiO_2 and high work-function noble metals resulting in a carrier-depleted interfacial region with an electric field that causes photogenerated holes to transfer to the noble metal and photogenerated hot and equilibrated electrons to be injected into or retained in TiO_2 (Fig. S1 in the ESI†). Cu-containing metallic and bimetallic photocatalysts are interesting for three reasons – the excellent selectivity toward specific photocatalytic reactions such as water-splitting and CO_2 photoreduction,[1,30–33] the lower cost of copper and the possibility of visible light absorption in Cu-based photocatalysts.[34,35] Cu–TiO_2 catalysts have been used in a wide variety of industrial reactions[36,37] such as the hydrogenation of 1,3-cyclooctadiene and the CO–NO reaction. It is noteworthy that very high performance has been reported for CuPt–TiO_2 hybrid photocatalysts in both oxidative and reductive reactions.[38,39]

There is some evidence in the scientific literature that TiO_2 forms Schottky junctions with noble metals such as Au and Pt.[40,41] These are also borne out by numerous recent reports of hot electron transfer from noble metals into TiO_2 and concomitant photoelectrochemical or photocatalytic activity but mostly without quantification of the Schottky barrier heights involved.[42–49] On the other hand, femtosecond transient absorption spectroscopy, surface potential imaging and electron spin resonance studies suggest the transfer of the photoexcited electron to the noble metal leaving the photogenerated hole in TiO_2.[24,50,51] Thus there exists a fundamental contradiction between the above two scenarios that needs resolving. Some reports claim that Pt NPs on *n*-TiO_2 act as electron sinks through Schottky barrier electron-trapping,[52,53] which represents a lack of understanding of the difference between the two scenarios outlined. Furthermore, the photocatalytic activity is highly sensitive to the method of formation and deposition of the noble metal NPs. Since NTs differ in the structure and properties from NPs, investigations into electronic interactions and charge transfer at the co-catalyst-TiO_2 interface specific to the 1-D nanostructures and the type of co-catalyst loading are quite important from the point of view of understanding and improving photocatalytic performance. The present study investigates the structure and electronic interactions at the CuPt NP–TTNTA hybrid interface wherein the CuPt NPs are photodeposited onto the nanotube walls, and compares them to the electronic properties of Sput-CuPt–TTNTA hybrids wherein the noble metal nanoparticles are formed by sputtering followed by thermal dewetting. Transparent nanotubes on FTO-coated glass substrates are used in this study since they allow clear and quantitative measurements of the effect of CuPt loading on the optical absorption of the photocatalyst.

Results and discussion

1. Morphology, structure and optical absorption of CuPt coated TTNTAs

MicroRaman spectroscopy is a sensitive and powerful technique to investigate defects, variations in the local structure and phase transformations in TiO_2 based materials. The Raman spectra of TTNTAs and CuPt–TTNTA hybrids are shown in Fig. 1. TTNTAs formed after anodization are amorphous in nature and their crystallization is achieved by annealing in air at 550 °C. For the crystalline anatase TiO_2 phase, six Raman active phonon modes are present that correspond to A_{1g}, B_{1g} and E_g modes, respectively. Fig. 1a shows a comparison of the Raman spectra of TTNTAs and CuPt–TTNTA hybrids. Raman spectra confirm the tetragonal anatase mode of TTNTAs with the presence of Raman active A_{1g}, B_{1g} and E_g modes.[54,55] It can be seen that the most intense peak for TTNTAs appears at 130.4 cm^{-1} corresponding to the E_g mode. In addition to the E_g mode, the other less intense peaks can be seen at 393.7 cm^{-1}, 513.1 cm^{-1} and 636.5 cm^{-1} confirming the presence of B_{1g}, A_{2g} and E_g modes, respectively. A shift in a peak position of 7 cm^{-1} (137 cm^{-1}) is found for CuPt–TTNTA hybrids for the main E_g mode with a small broadening. This shift in CuPt–TTNTA hybrids is due to the dispersion of bimetallic CuPt NPs over TiO_2 producing a change in the local structure of TiO_2. Fig. 1b shows the Raman spectra of CuPt–TTNTA hybrids subjected to different irradiation times by the one sun output of a calibrated solar simulator together with heating at 100 °C. Such a configuration to study the CuPt–TiO_2 interface was chosen keeping in mind the fact that both photochemical and thermochemical interfacial reactions are possible upon illumination in TTNTA photocatalysts. The inset of Fig. 1b shows the broadening of the main E_g peak in the case of hybrids irradiated with different times in correspondence to the TTNTAs, which we associate with increasing structural disorder upon prolonged exposure to ultraviolet photons in simulated sunlight.

The UV-Vis spectra in Fig. 1c show a strong sub-bandgap absorption in the bare TTNTAs due to an extended Urbach tail.

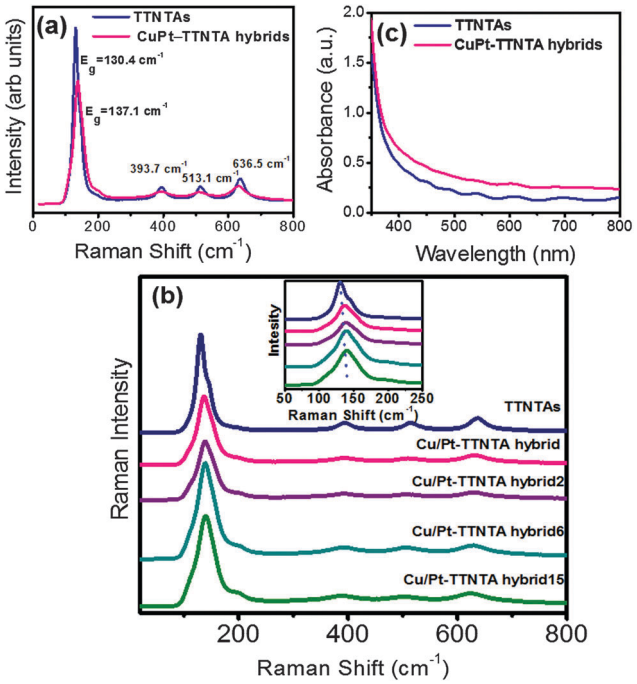

Fig. 1 Counter-clockwise from top-left, (a) comparison of the room temperature Raman spectra of TTNTAs and CuPt–TTNTA hybrids, (b) microRaman spectra of CuPt–TTNTA hybrids heated to 100 °C with different light exposure times, here 2, 6 and 15 correspond to hours of illumination; the inset figure shows the broadening in the E_g peak of TiO_2 with time. (c) UV-Vis spectra of TTNTAs and CuPt–TTNTA hybrids.

No pronounced additional optical transitions were found in the CuPt–TTNTA hybrids. Intra- and interband absorption in CuPt NPs resulted in a slightly increased absorption of light throughout the visible spectral range in CuPt–TTNTA hybrids in comparison to TTNTAs. The morphology of the as-prepared TTNTAs was imaged using FESEM (Fig. S2 in ESI†) where close packed TTNTAs with an average outer diameter ~105 nm are seen. An inset image in the top left corner of Fig. S2a in the ESI,† shows a cross section of TTNTAs with a tube-length of 1 μm. Not much change is observed in the morphology of TTNTAs after CuPt loading. The nanoparticles of bimetallic alloys that form CuPt–TTNTA hybrids are too small to be seen in SEM images. Low and high resolution-TEM images and EDAX spectra of TTNTAs and their hybrids are displayed in Fig. 2. A direct attachment of CuPt-NPs is clearly seen along the walls of TiO_2 nanotubes (Fig. 2a). The encircled regions in this image show CuPt NPs that are 2–5 nm in diameter, which is further confirmed through HRTEM images (Fig. 2c). However, there likely are several NPs similar in size to, or just below, the microscope resolution limit of 1 nm. The presence of these is inferred through features in the electronic spectra discussed later in this report.

A high angle annular dark field scanning TEM (HAADFSTEM) image, shown in Fig. 2b corresponds to the tiny bright spots demonstrating the dispersion of CuPt NPs on TTNTAs. A close knit attachment of CuPt NPs with the TTNTAs can be seen in Fig. 2c, favoring the CuPt NPs and TiO_2 nanotube array structures to form hybrids with a strong interaction. EDX spectra, shown in Fig. 2d confirm the elemental state of Pt only, due to a very small concentration of Cu. However, the HRTEM images shown in Fig. 3 confirm the presence of a CuPt bimetallic alloy. Fig. 3a–c display the auto correlated lattice spacing, analyzed from HRTEM pictures. The anatase phase of TiO_2 with a *d*-spacing of 0.34 nm corresponding to the (101) plane is confirmed through high resolution lattice fringes (Fig. 3a). The presence of Pt and CuPt alloys is also confirmed from the *d*-spacing of the lattice fringes to be 0.24 nm (111) and 0.22 nm (111), respectively (Fig. 3b and Fig. 3c). The *d*-spacing of 0.22 nm from the lattice fringes reveals the formation of a Pt rich alloy with very small concentrations of Cu. A complete chain of TTNTAs and the CuPt–TTNTA hybrids with their corresponding *d*-spacing is summarized in Fig. 3d. Thus HRTEM results confirm the intimate nature of the CuPt–TiO_2 hybrid structure interface that is the foundation for the further set of studies.

2. Elemental composition and photoemission spectra of CuPt–TTNTA hybrids

XPS, which is a highly surface sensitive technique, was performed to investigate the difference in the chemical states of different elements present in TTNTAs and CuPt–TTNTA hybrids. XPS is also used as a means to understand the charge transfer and electronic interactions between the metal and the support in the mentioned hybrid structure (Fig. 4b–d). The survey scans on TTNTAs and CuPt–TTNTA hybrids confirmed the presence of Ti, O and Pt. The Cu peak was not observed in the XPS survey scans owing to its very small concentration. To confirm the presence of Cu, time of flight-SIMS in the depth profiling mode was performed on the sample that confirmed the presence of Cu by mass (Fig. 4a).

TOF-SIMS spectra (Fig. 4a) confirm the presence of all the materials present in the sample along with the substrate up to a sputtering time of ~2600 s, which corresponds to the transition from the TiO_2 nanotube barrier layer to the FTO layer below. Furthermore, the intensities of Cu and Pt obtained through SIMS profiling correlate well with that of Ti, indicating a fairly uniform loading of CuPt NPs along the nanotube walls with a slight increase in Pt concentration closer to the barrier layer. The core level spectra of Ti, O and Pt are seen in Fig. 4b–d. In Fig. 4b, the Ti $2p_{3/2}$ and Ti $2p_{1/2}$ states in TTNTAs present at 458.4 eV and 464.2 eV, respectively, correspond to Ti^{4+} states.[56] The Ti^{4+} surface state shifts to 457.8 eV and 463.5 eV in CuPt–TTNTA hybrids. Fig. 4c displays the O 1s spectra with the presence of a Ti–O peak at 529.63 eV and 529.45 eV for TTNTAs and for CuPt–TTNTA hybrids, respectively. While the binding energy shift in this case appears to be a mere −0.18 eV, measurements over a number of samples and peak decomposition of the resulting O 1s spectra show that TTNTAs without an oxygen plasma treatment exhibit peaks at 531.90 eV and 530.14 eV, which correspond to O–Ti (3+) and HO–Ti (3+) respectively (Fig. S5 in the ESI†). Oxygen plasma treatment of the surface changes the relative weighting of the two peaks but leaves the peak positions almost unchanged (Fig. S5 in ESI†). On the other hand, photodeposition of CuPt consistently shifts both the peaks constituting the O 1s spectrum to lower binding energies (top panel of Fig. S6 in ESI†).

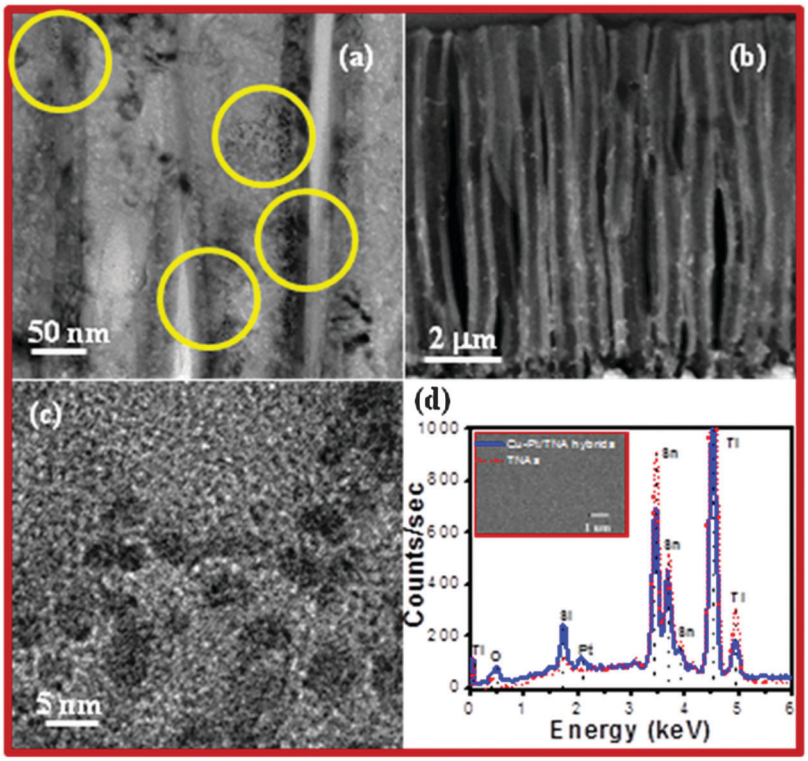

Fig. 2 Low and high resolution transmission electron microscope images showing (a) CuPt nanoparticle loaded TTNTAs, (b) HAAFD image in the STEM mode presenting the CuPt–TTNTA hybrids, (c) close knit attachment of CuPt nanoparticles along the walls of TTNTAs and (d) EDAX spectra confirming the presence of Pt.

This shift to lower binding energies after CuPt loading is characteristic of n-type semiconductors forming a Schottky junction with high work function metals, and occurs as a result of the lattice distortion of the TiO_2 surface that generates oxygen vacancies. The oxygen vacancies in TiO_2 correspond to the formation of Ti^{3+} states. Such a charge transfer process results in the shifting of binding energy of Ti to the lower energy side in CuPt–loaded TTNTAs. Measurements of multiple CuPt–TTNTA hybrid samples yielded a band bending of 0.4–0.7 eV from the shifts in the Ti 2p core-level spectra. The Pt 4f spectra can exhibit both initial and final state effects. The electric field due to the depletion region shifts the $4f_{7/2}$ and $4f_{5/2}$ peaks at 71.0 eV and 74.4 eV in bulk Pt to lower binding energies while the size-dependent screening effect shifts the peaks to higher binding energies. The width (FWHM) of the Pt $4f_{7/2}$ peak in bulk Pt is smaller than 0.5 eV. However, in Fig. 4d and for other samples of photodeposited CuPt–TTNTA hybrids (see Fig. S8a in ESI†), the FWHM is *ca.* 1.5 eV which is indicative of the presence of Pt clusters of size 1 nm and smaller.[57] In Fig. 4d, the binding energy shifts in the two Pt 4f peaks are +0.2 to +0.4 eV. However, for samples with band bending towards the lower end of the range (0.4–0.5 eV), the peak shifts are +1.2 to +1.5 eV as shown in Fig. S8a in the ESI,† which we attribute to the final state effect being less obscured by the initial state effect.[57] The data obtained by us strongly indicate that metallic behavior is not fully developed in the photodeposited CuPt nanoparticles.

2.1 Band alignment in CuPt coated TTNTAs. A clear difference in the UPS spectra of transparent TiO_2 nanotubes before and after the photodeposition of CuPt nanoparticles is evident in Fig. 5 with both the secondary electron cut-off and the valence band edge red-shifted to lower binding energies. The valence band maximum, which was previously located 3.25 eV below the Fermi level (E_f), is shifted to 2.76 eV below the Fermi level. By examining UPS spectra from multiple CuPt–TTNTA hybrid samples, a range of 0.49–0.67 eV was obtained for the observed band bending following CuPt photodeposition. The close agreement between the band-bending values obtained from XPS core-level spectra and UPS valence band spectra is noteworthy, and confirms the formation of a depletion region at the CuPt–TiO_2 interface following photodeposition. The resolution of the UPS spectra is slightly superior to that of XPS spectra (see Methods section) making the narrower UPS range more reliable. The work-function of a semiconductor surface is given by $\phi_s = h\nu - E_{SE}$ where the first term represents the energy of the photons used to probe the band-structure ((He I:21.21 eV) in our case) and the second term is the secondary electron cut-off energy. The work function of the transparent titania nanotubes is found to be 4.23 eV (implied electron affinity of 4.17 eV) in agreement with most prior studies on anatase thin films and nanostructures,[58,59] and increased by 0.36 eV upon photodeposition of CuPt to 4.59 eV. The difference of 0.13–0.31 eV between the estimated band-bending and the change in work-function indicates the formation of a surface dipole (Δ) at the CuPt nanoparticle-decorated TiO_2 surface (see Fig. S1 in the ESI†).[60]

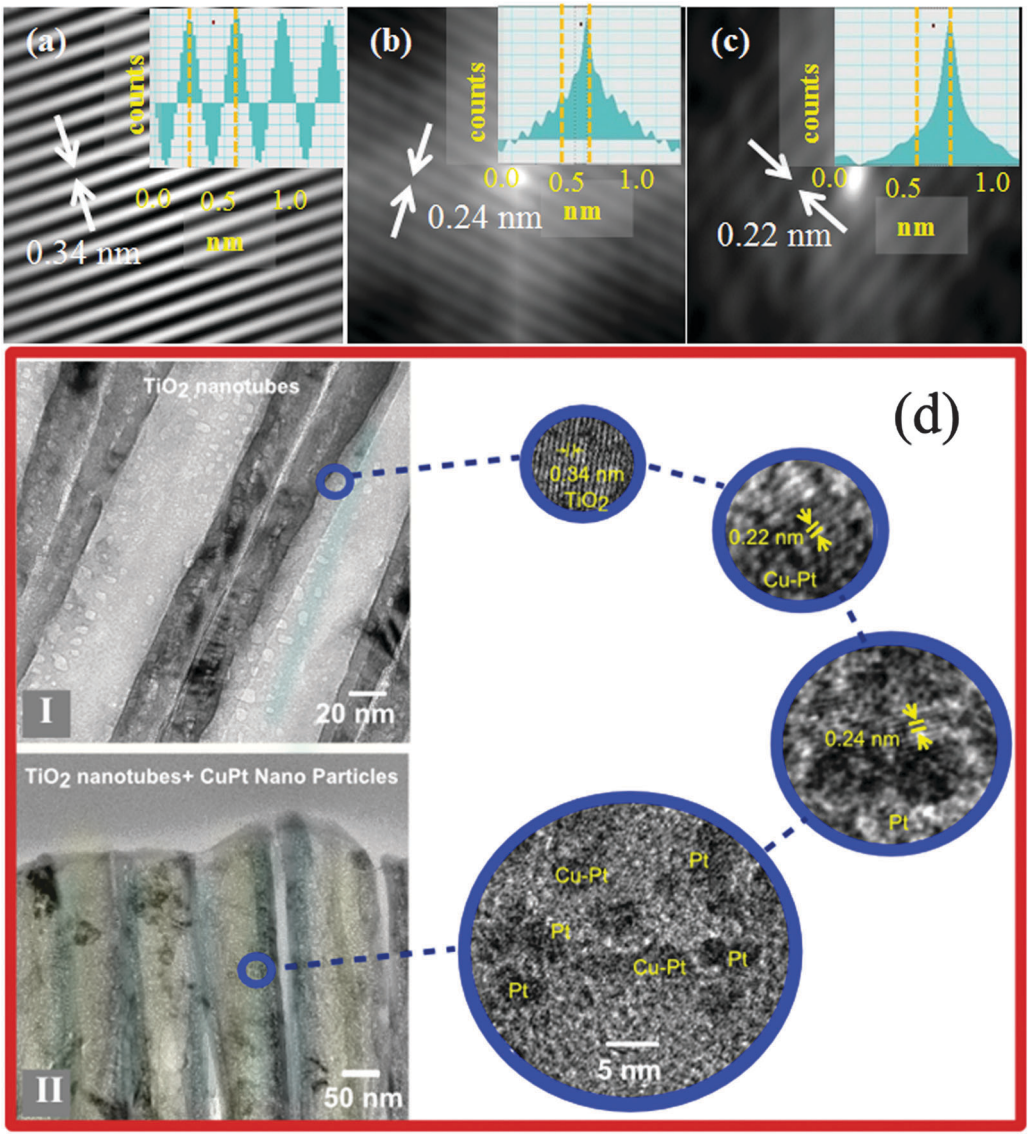

Fig. 3 High-resolution autocorrelated images of (a) TiO_2 lattice planes, (b) Pt NPs, (c) CuPt NPs, (d) HRTEM images displaying the crystalline planes for (I) TTNTAs and (II) CuPt–TTNTA hybrids.

To understand the effect of Cu in CuPt–TTNTA hybrids, UPS data were collected from Pt–TTNTA hybrids wherein TiO_2 nanotube arrays were coated with monometallic Pt nanoparticles using a near-identical photodeposition process. These data (see Fig. S12 in the ESI†) indicate the valence band edge in Pt–TTNTA hybrids to be shifted upward toward to the Fermi level by a much larger amount than in CuPt–TTNTA hybrids indicating a band bending as large as 1.6 eV. This observation can be rationalized using the Anderson model[29] based on the much higher work function of monometallic Pt which is reduced by the addition of Cu in bimetallic alloys.

2.2 Examination of the effect of illumination in pure methanol on the TiO_2 surface. Photodeposition was performed by us in a methanolic medium and involved the photocatalytic reduction of the noble metal precursors (acetylacetonate salts of Cu and Pt). A question that arises is whether the TiO_2 nanotubes also experience the chemical reduction of the surface during this process through the ultraviolet photon-mediated photocatalytic oxidation of methanol. The significance of this question lies in the determination of whether the observed Ti^{3+} states in CuPt–TTNTA hybrids arise from charge transfer to the metal or from reduction by methanol. Therefore photoemission spectroscopic measurements were performed in methanol under identical conditions without the metal precursors, and the resulting spectra were compared to TTNTAs and CuPt–TTNTA hybrids. The UPS spectra of methanol illuminated samples (Fig. 6) are very dissimilar to those of TTNTAs and CuPt–TTNTA hybrids (Fig. 5) with regard to the shape and locations of peaks and energy cut-offs. The valence band maximum for the methanol illuminated transparent titania nanotube array samples occurred at 3.10 eV, indicating a maximum band-bending of 0.15 eV produced by the chemical reduction of the TiO_2 surface.

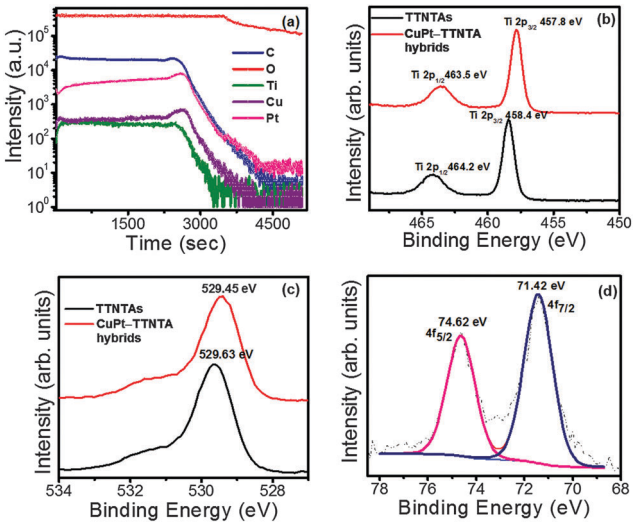

Fig. 4 TOF-SIMS and XPS data from CuPt–TTNTA hybrids (a) TOF-SIMS and core-level spectra of (b) Ti 2p (c) O 1s and (d) Pt 4f.

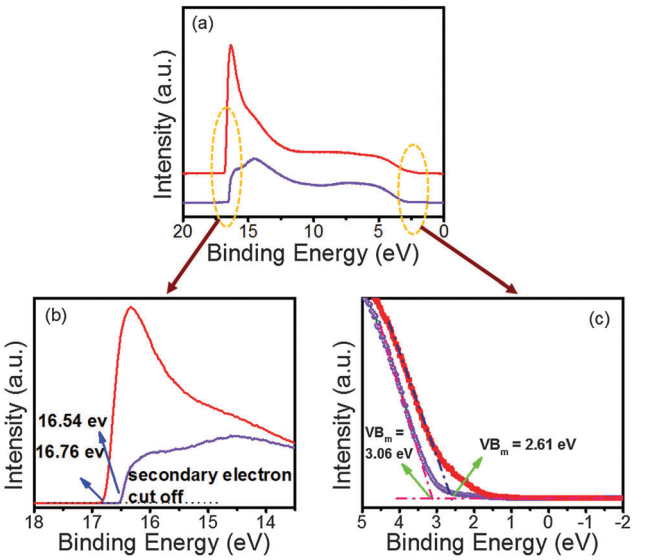

Fig. 6 Counter-clockwise from top (a) whole UPS spectra (b) magnified view of the secondary electron cut-off region and (c) valence band edges of transparent TiO_2 nanotube samples following the photodeposition of CuPt NPs (red curve) subsequent to illumination under identical conditions in methanol but without the presence of metal precursors (purple curve).

Under the same sample preparation and illumination conditions, the valence band maximum for CuPt–TTNTA hybrids occurred at 2.76 eV. As seen in Fig. S7 in the ESI,† transparent TiO_2 nanotube samples illuminated in methanol under identical conditions but without the metal precursors do not show a shift unlike the CuPt–TTNTA hybrids in Fig. 5. Thus significant band bending is indicated only in the presence of CuPt nanoparticles. The increase in the work function of the methanol illuminated samples implied by the secondary electron cut-offs occurring at lower binding energies in the UPS spectrum of Fig. 6b is attributed to surface adsorbates formed during the photochemical oxidation of methanol. The detailed study of

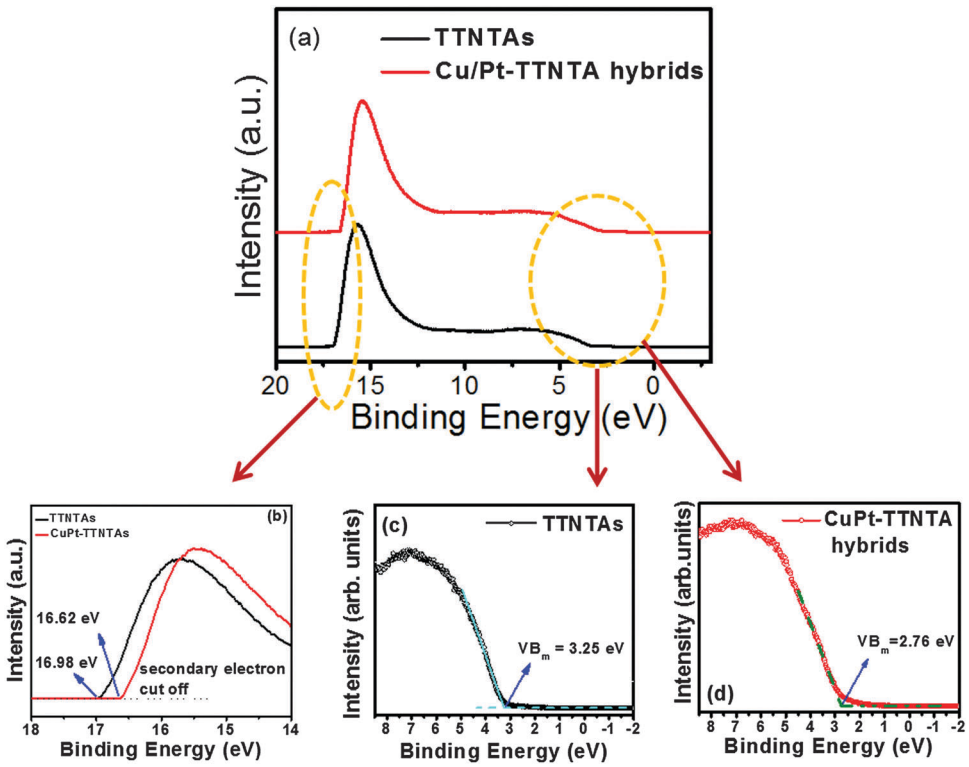

Fig. 5 UPS spectra of CuPt–TTNTA hybrids. For each spectrum, the valence band maximum was estimated using the intercept on the abscissa obtained by extrapolating the low binding energy edge to the baseline.

such adsorbates is outside the scope of this work, but we will mention here that the dramatic attenuation of the secondary electron emission peaks in Fig. 6a is a well-known sign of the presence of such adsorbates.[61,62]

The deposition of CuPt nanoparticles is not purely a chemical reduction of the complexed Cu(II) and Pt(II) species in the respective acetylacetonates because the presence of ultraviolet radiation is essential. Therefore, the reaction is photo-induced, and it is possible to have one or both of photochemical reduction and photocatalytic deposition.[63] In photochemical reduction, the illuminated solvent (MeOH, a potent hole scavenger) is the reducing agent and it is conceivable that the TiO_2 too gets reduced in addition to the Cu(II) and Pt(II) ions. On the other hand, in photocatalytic deposition, it is illuminated TiO_2 that is the reducing agent (through photogenerated electrons). Therefore, TiO_2 can get oxidized at best but is more typically unchanged (since the reduction is performed by photogenerated excess charge carriers).[56] The data presented here enable clear differentiation between the two phenomena under consideration. In particular, the band alignments produced by the photodeposition of CuPt on TiO_2 nanotube arrays are shown to be totally different from the corresponding alignment produced by a pure photochemical reaction in methanol.

2.3 Comparison of photodeposited CuPt NPs with sputtered CuPt NPs. Fig. 7 displays the transformation in the UPS valence band spectra of transparent TiO_2 nanotubes after the formation of 2–5 nm sized CuPt nanoparticles by sputtering. The morphology and structure of such vacuum deposited mono- and bimetallic noble metal nanoparticles deposited onto one-dimensional titania nanostructures have been reported on elsewhere.[24,64–66] For sputtered CuPt, the UPS spectra at low binding energies show a clear Fermi edge close to E_f = 0 eV, which is a strong manifestation of metallic behavior. Likewise, the Pt 4f spectra in Fig. S8b (in the ESI†) show peaks at 71.0 eV and 74.4 eV corresponding to those of bulk platinum. These findings are in line with prior reports that show the metallic behavior of metal-semiconductor heterojunctions dominating at metal coverages exceeding 2 nm. The FWHM of the Pt $4f_{7/2}$ peak is ~1 eV for the sputtered CuPt NPs, less than that of photodeposited CuPt NPs by ~0.5 eV but not quite approaching the value of bulk Pt (0.5 eV). In Fig. 7, the valence band of TiO_2 is not completely obscured by the metallic behavior and is seen to be mostly unchanged by the formation of a heterojunction with sputtered CuPt. Furthermore, Fig. S9 (in the ESI†) highlights the vast differences in the low binding energy XPS spectra of Sput-CuPt–TTNTA hybrids and the other types of TTNTAs studied in this report. CuPt–TTNTA hybrids formed by photodeposition show a rich collection of features in the 0–60 eV binding energy range, rather similar to those exhibited by TTNTAs subjected to ultraviolet radiation in methanol albeit shifted. However, these features in the 0–60 eV spectral range are mostly absent or smeared out for the Sput-CuPt–TTNTA hybrids in Fig. S9 (in the ESI†), which provides further confirmation of the manifestation of bulk metallic behavior in the sputtered samples and the lack thereof in the photodeposited samples. In Fig. 7d, the Ti 2p binding energies for Sput-CuPt–TTNTA hybrids are slightly blue-shifted by 0.3 eV from the corresponding binding energies observed for bare TTNTAs in Fig. 4b. In the absence of concomitant shifts in the Pt 4f spectra (Fig. S8b in ESI†) to support the formation of an accumulation layer (downward band-bending), such a shift may indicate a healing of the TiO_2 surface by scavenging of remnant Ti^{3+} species by the deposited noble metal nanoparticles. Thus, the sputtered CuPt nanoparticles certainly do not exhibit upward band-bending (*i.e.* depletion) as manifested by shifts in either core-level spectra or the valence band spectra.

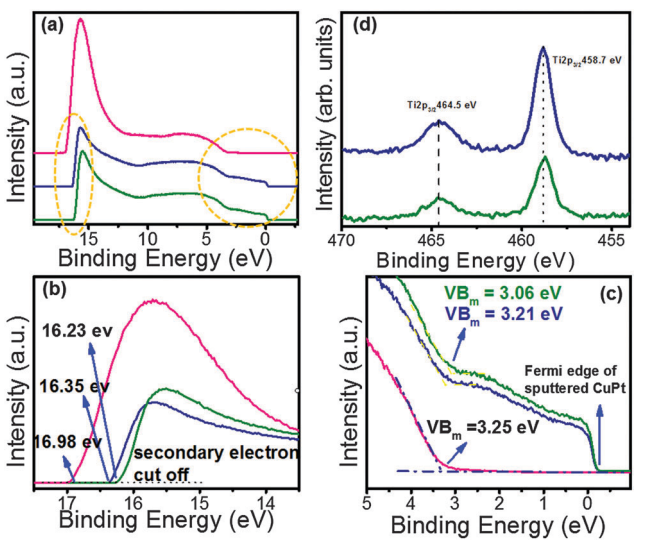

Fig. 7 Counter-clockwise from top-right (a–c): survey and magnified UPS valence band spectra of transparent TiO_2 nanotubes (pink-colored curve), sputtered CuPt nanoparticles formed on transparent TiO_2 nanotubes subsequent to oxygen plasma clean (green-colored curves) and sputtered CuPt nanoparticles formed on transparent TiO_2 nanotubes without an oxygen plasma clean (blue-colored curves). In (d), the high resolution XPS core-level spectra of the Ti 2p peak are shown for sputtered CuPt nanoparticles formed on TiO_2 nanotube arrays.

The study of the interfacial band alignment in TTNTA:CuPt hybrids was accompanied by CO_2 photoreduction studies and was compared with Sput-CuPt–TTNTA hybrids. Fig. 8a illustrates a photoreactor used for the reduction studies and the mechanism for a photoreduction process. The photoreduction of CO_2 to CH_4 is a complex that involves at least eight electron transfer steps. TTNTA:CuPt NPs demonstrated a higher CH_4 yield (~600 nmol cm^{-12} h^{-1}) in comparison to TTNTAs coated with sputtered CuPt (~30 nmol cm^{-2} h^{-1}) for 6 hours of illumination under AM 1.5 one sun illumination, in agreement with previous reports.[22,64] More details related to how this experiment was performed are provided in the ESI.† Despite CuPt–NPs not acting as electron sinks at moderate illumination intensities, such TiO_2 nanotube–CuPt NP heterojunctions have demonstrated excellent performance for both photooxidation and photoreduction reactions. We hope our results will highlight the importance of the preparation technique on band alignment in heterojunctions and stimulate the search for reaction mechanisms where noble metals behave as hole-sinks.

2.4 Work functions, Schottky barriers and surface dipoles at TiO_2 nanotube surfaces. A number of samples examined in this study exhibit divergent behavior in their work-functions

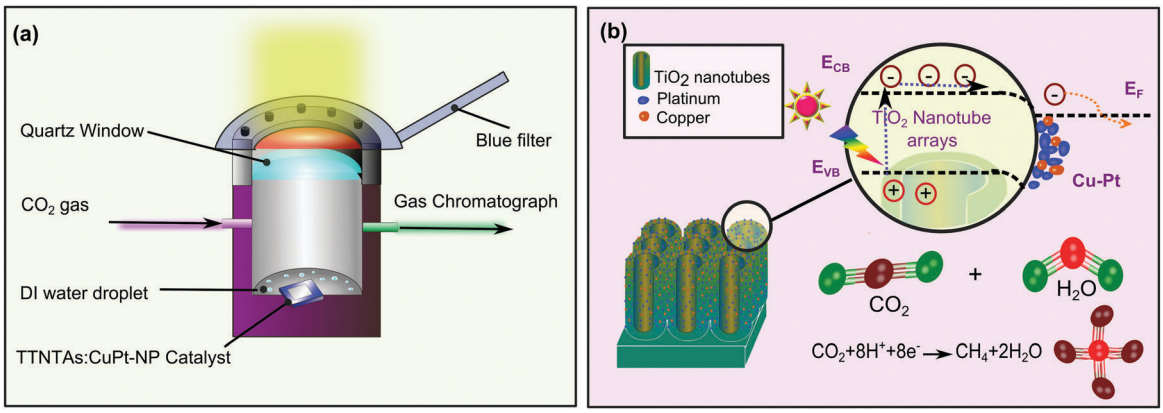

Fig. 8 Schematic illustrations displaying the (a) photoreactor used for reduction experiments using TTNTA:CuPtNP hybrids as photocatalysts for the sunlight-driven conversion of CO_2 into methane and (b) the conventional mechanism used to explain the conversion of carbon dioxide to methane by photoreduction on TiO_2.

(as obtained from the secondary electron cut-off in the UPS spectra) and their band-bending (as obtained from shifts in the core-level binding energies and the UPS valence band edges). For instance, TTNTA samples were illuminated by UV photons in methanol (Fig. 6c), the valence band edge is slightly red-shifted by 0.19 eV to 3.06 eV from 3.25 eV in TTNTAs (Fig. 5c) but with a red-shift of 0.44 eV in the secondary electron emission cut-off from 16.98 eV (Fig. 5b) to 16.54 eV (Fig. 7b). Therefore, the change in the work-function is significantly larger than the magnitude of the band-bending, and indicates the formation of a −0.25 eV surface dipole. The surface dipole does not affect the core-level binding energies of photoelectrons generated interior to itself.[67] The absence of exact correlation between the work-function and the band-bending may be related to the orientation sensitivity of the work-function and the charge transfer.[68] In polycrystalline TiO_2 nanotube arrays, the crystal planes exposed to the vacuum that determine the work function can be different from the crystal planes which have contributed to the bulk of the transferred electronic charge. Sput-CuPt–TTNTA hybrid samples too exhibit significant shifts to higher work-functions with small or negligible band bending. However, these samples also show prominent bulk metallic character in their UPS spectra as manifested by their Fermi edges. Therefore the work functions of 4.86–4.98 eV measured here (Fig. 7c) are that of the bimetallic nanoparticles, and explained by the reduction of the platinum work-function of 5.5 eV due to the addition of lower work-function copper (φ_{Cu} = 4.6 eV).

The Schottky barrier height is given by $\Phi_B = \phi_{bi} + \phi_n$ where ϕ_n ($E_C - E_F$) depends on the intrinsic carrier concentration in the n-TiO_2 nanotubes and ϕ_{bi} is the maximum band-bending in the semiconductor. ϕ_{bi} is given by $kT \ln N_c/n$ where k is Boltzmann's constant and T is the absolute temperature, and estimated to be 0.06 eV at room temperature based on a conduction band density of states (N_c) of 10^{21} cm^{-3}. In this study, we used TiO_2 nanotubes formed in ethylene glycol electrolytes and annealed in air, for which a carrier concentration (n) in the range 1.4×10^{19}–3.5×10^{20} cm^{-3} has been measured.[69,70] The bandgap (E_g) of anatase phase TiO_2 nanotubes (3.32 eV) is known to be slightly larger than that of bulk anatase.[32,71] Thus, a range of 0.55–0.73 V is estimated for the Schottky barrier height. For a point-contact Schottky diode such as the one formed by isolated CuPt NPs decorating the walls of titania nanotube arrays, a hemispherical depletion region is obtained as shown in Fig. S10 (in the ESI†).[72] We extracted the depletion region widths of such point-contact Schottky junctions with a barrier height of 0.4–0.7 V for 1 nm, 2 nm and 5 nm sized metal NPs for a range of equilibrium carrier concentrations in n-TiO_2 (Fig. S11 in the ESI†). The resulting depletion widths are 2–10 nm (the inset of Fig. S11 in the ESI†). Since the wall-thickness of the TiO_2 nanotubes is in the range 25–35 nm (see Fig. 2 and 3), the nanotubes will not be fully depleted by the surface band bending.

2.5 Schottky barrier electron trapping? Internal electric fields are vital in photocatalysts to separate charge carriers so that photogenerated electrons and holes drive chemical reactions instead of being lost to recombination. The electronic band-alignment at the support-promoter hetero-interface is needed in order to understand the correct photocatalytic mechanism of operation and also to improve the catalytic activity. The magnitude and direction of electric fields in a vast majority of photocatalysts based on n-type anatase-phase TiO_2–noble metal nanoparticle (nm-NP) heterojunctions are undetermined yet an assumption is made in many reports that nm-NPs act as sinks for photo-generated electrons while photo-holes remain in TiO_2 based on spectroscopic evidence in a restricted set of idealized TiO_2–noble metal junctions where the noble metal is deposited by high vacuum deposition. The term "Schottky-Barrier Electron Trapping" is used quite frequently in the photocatalytic literature to describe the electron sink effect of noble metal nanoparticles.[73–77] But a Schottky barrier would indicate electron transfer to surface reactants on TiO_2 surfaces and hot hole injection into the CuPt NPs where they might participate in further reactions,[78] opposite to the aforementioned electron sinking effect. At moderate incidence intensities of supra-bandgap photons (a carrier generation rate $< 10^{19}$ cm^{-3}), the term "Schottky-barrier electron trapping" would be wholly incorrect due to its implication that noble metal nanoparticles trap photogenerated

electrons due to the built-in field of the Schottky junction when it is actually photogenerated holes that would be trapped by the noble metal. At high illumination intensities, flat band conditions are created which may favor electron trapping at the noble metal due to kinetic rather than energetic conditions if the hole is scavenged quickly enough by surface-bound species. But the electron trapping here would occur due to kinetic factors rather than the Schottky barrier. Likewise flat band conditions exist in very small anatase nanoparticles ($r < 20$ nm) with a relatively low intrinsic carrier concentration that are unable to support a depletion region. But flat band conditions are unlikely to prevail in larger-sized, moderately-to heavily n-type TiO_2 crystallites or on single crystal anatase surfaces. Therefore we suggest that the term ''Schottky-Barrier Electron Trapping'' be used with extreme caution with n-type semiconductor photocatalysts if used at all.

In the conventional understanding of photocatalysis, noble metal NPs act as electron sinks[79,80] due to which the transfer of photogenerated electrons to reactants occurs primarily on metal surfaces while the high oxidizing power of photogenerated holes is used in reactions on TiO_2 surfaces. The efficiency of charge-separation processes in such a scenario is kinetically controlled by parameters such as the minority carrier diffusion length, the photoinduced electron transfer rate to the metal, trapping cross-sections and time-constants, *etc.* However, our XPS studies of the CuPt–TiO_2 interface in transparent TiO_2 nanotube arrays (TTNTAs) coated with photodeposited CuPt NPs (CuPt–TTNTA hybrids) show the existence of a depletion region with a built-in potential of 0.49–0.67 V. Under actual photocatalytic reaction conditions, further variation of the interfacial electronic properties is possible due to the adsorption of reactant species. Notwithstanding this, the Schottky barrier at the CuPt–TiO_2 interface detected by our studies would direct photoexcited electrons toward the TiO_2 and photoexcited holes toward the CuPt NPs (Fig. S1 in ESI†), which would require a review of the commonly accepted mechanistic routes for various photocatalytic reactions that are almost exclusively based on hole-mediated oxidation on TiO_2 and electron-mediated reduction on the noble metal surface. The conventional model of noble metal electron sinks may still be applicable to the case of Sput-CuPt–TTNTA hybrids for which upward band bending was not detected.

Conclusions

The structure and electronic properties of the TiO_2–noble metal interface are important in both photocatalysis and conventional catalysis. Most of the work in this area considers single crystals of rutile – reports on other forms and phases of TiO_2 are scarce. Likewise, the majority of photoemission spectroscopic studies consider metal nanoparticles or films deposited under high vacuum conditions. However alternative methods of noble metal impregnation such as electrodeposition, photodeposition, wet impregnation, deposition–precipitation and colloidal synthesis are being extensively used to prepare photocatalysts, and the electronic properties of the resulting interfaces with semiconductor supports are largely unknown. Anodically formed TiO_2 nanotube arrays coated with noble metal nanoparticles (NPs) formed by non-vacuum processes are being researched intensively for photocatalytic applications and have shown exceptional performance in recent studies. Cu–Pt bimetallic nanoparticles (NPs) were decorated over transparent TiO_2 nanotube arrays *via* a facile approach of photodeposition to investigate their influence on the structural and electronic properties of CuPt–TTNTA hybrids. HRTEM studies revealed that Cu–Pt NPs were closely attached to the walls of TiO_2 nanotubes. The crystalline structure of nanotubes and the local changes at the interface of CuPt–TTNTA hybrids were confirmed by microRaman spectroscopy. A shift in the E_g Raman mode along with a narrow broadening for CuPt–TTNTA hybrids was found due to the dispersion of bimetallic CuPt nanoparticles over TiO_2 nanotubes. The lack of manifestation of metallic behavior in the XPS and UPS spectra was used to infer that the majority of photodeposited CuPt NPs had a size of 1 nm or smaller, even though 2–5 nm NPs were detected in electron micrographs. On the other hand, 2–5 nm sputtered and thermally dewetted CuPt manifested clear metallic behavior. The formation of a Schottky barrier at the CuPt–TiO_2 interface with a band bending of 0.49–0.67 eV was confirmed through XPS and UPS studies in the photodeposited CuPt–TTNTA hybrids in comparison to sputtered CuPt–TTNTA hybrids, where no appreciable band bending was present. A close agreement between the band-bending values obtained from XPS and UPS results corroborates the formation of a depletion region at the photodeposited Cu–Pt TiO_2 nanotube interface. This study also points to the strong effect of the preparation conditions of the noble metal promoter on the electronic structure of the resulting photocatalyst. We show that sputtered CuPt and photodeposited CuPt have substantially different band-alignment in heterojunctions with TiO_2 nanotubes. Photochemical reduction by methanol was ruled out as a cause for the observed difference. On the other hand, the different size-scales of the sputtered and photodeposited CuPt nanoparticles were shown to be a contributing factor. Finally, the errors associated with the use of the term ''Schottky barrier electron trapping'' were highlighted.

Acknowledgements

This project was funded through grants from the National Research Council of Canada (NRC) and NSERC. Some device fabrication and testing used research infrastructure made possible by a Leaders Opportunity Fund grant to K.S. from the Canada Foundation for Innovation (CFI) and the Alberta Small Equipment Grants Program (SEGP). Equipment use and staff assistance at the UofA NanoFab and the Alberta Centre for Surface Engineering and Science (ACSES) is acknowledged along with the funding obtained for user fees from CMC Microsystems. Measurement of the work functions and optical spectra of some samples by Ahmad Adl, synthesis of some TTNTAs by Abdelrahman Askar, and design of photocatalytic

reactor and some CO_2 photoreduction measurements by Xiaojiang Zhang are acknowledged. We also thank Prof. Jillian Buriak for helpful discussions.

References

1 K. Shankar, J. I. Basham, N. K. Allam, O. K. Varghese, G. K. Mor, X. J. Feng, M. Paulose, J. A. Seabold, K. S. Choi and C. A. Grimes, *J. Phys. Chem. C*, 2009, **113**, 6327–6359.
2 T. E. Mallouk, *J. Phys. Chem. Lett.*, 2010, **1**, 2738–2739.
3 H. H. Mohamed and D. W. Bahnemann, *Appl. Catal., B*, 2012, **128**, 91–104.
4 S. Valencia, F. Cataño, L. Rios, G. Restrepo and J. Marín, *Appl. Catal., B*, 2011, **104**, 300–304.
5 K. Li, X. An, K. H. Park, M. Khraisheh and J. Tang, *Catal. Today*, 2014, **224**, 3–12.
6 J. Pan, X. Wu, L. Wang, G. Liu, G. Q. Lu and H.-M. Cheng, *Chem. Commun.*, 2011, **47**, 8361–8363.
7 Q. Zhai, S. Xie, W. Fan, Q. Zhang, Y. Wang, W. Deng and Y. Wang, *Angew. Chem., Int. Ed.*, 2013, **52**, 5776–5779.
8 A. Mohammadpour, P. Kar, B. D. Wiltshire, A. M. Askar and K. Shankar, *Curr. Nanosci.*, 2015, **11**, 593–614.
9 Q. Zhang, V. Celorrio, K. Bradley, F. Eisner, D. Cherns, W. Yan and D. J. Fermín, *J. Phys. Chem. C*, 2014, **118**, 18207–18213.
10 J. R. Jennings, A. Ghicov, L. M. Peter, P. Schmuki and A. B. Walker, *J. Am. Chem. Soc.*, 2008, **130**, 13364–13372.
11 R. Mohammadpour, A. Iraji zad, A. Hagfeldt and G. Boschloo, *ChemPhysChem*, 2010, **11**, 2140–2145.
12 G. K. Mor, K. Shankar, M. Paulose, O. K. Varghese and C. A. Grimes, *Nano Lett.*, 2006, **6**, 215–218.
13 X. Feng, K. Zhu, A. J. Frank, C. A. Grimes and T. E. Mallouk, *Angew. Chem., Int. Ed.*, 2012, **51**, 2727–2730.
14 K. Zhu, N. R. Neale, A. Miedaner and A. J. Frank, *Nano Lett.*, 2006, **7**, 69–74.
15 M. H. Zarifi, A. Mohammadpour, S. Farsinezhad, B. D. Wiltshire, M. Nosrati, A. M. Askar, M. Daneshmand and K. Shankar, *J. Phys. Chem. C*, 2015, **119**, 14358–14365.
16 C. C. Mercado, F. J. Knorr, J. L. McHale, S. M. Usmani, A. S. Ichimura and L. V. Saraf, *J. Phys. Chem. C*, 2012, **116**, 10796–10804.
17 G. Mie, Contributions to the optics of turbid media, particularly of colloidal metal solutions Transl. into ENGLISH from Ann. Phys.(Leipzig), v. 25, no. 3, 1908, p. 377–445, 1976, **1**, 377–445.
18 R. Gans, *Ann. Phys.*, 1912, **342**, 881–900.
19 L. Li, P. A. Salvador and G. S. Rohrer, *Nanoscale*, 2014, **6**, 24–42.
20 N. T. Nguyen, M. Altomare, J. Yoo and P. Schmuki, *Adv. Mater.*, 2015, **27**, 3208–3215.
21 N. T. Nguyen, J. Yoo, M. Altomare and P. Schmuki, *Chem. Commun.*, 2014, **50**, 9653–9656.
22 X. Zhang, F. Han, B. Shi, S. Farsinezhad, G. P. Dechaine and K. Shankar, *Angew. Chem.*, 2012, **124**, 12904–12907.
23 B. Amirsolaimani, X. Zhang, F. Han, S. Farsinezhad, A. Mohammadpour, G. Dechaine and K. Shankar, *MRS Online Proc. Libr.*, 2013, **1578**, DOI: 10.1557/opl.2013.841.
24 W.-N. Wang, W.-J. An, B. Ramalingam, S. Mukherjee, D. M. Niedzwiedzki, S. Gangopadhyay and P. Biswas, *J. Am. Chem. Soc.*, 2012, **134**, 11276–11281.
25 X. J. Feng, J. D. Sloppy, T. J. LaTemp, M. Paulose, S. Komarneni, N. Z. Bao and C. A. Grimes, *J. Mater. Chem.*, 2011, **21**, 13429–13433.
26 K. S. Raja, Y. R. Smith, N. Kondamudi, A. Manivannan, M. Misra and V. Subramanian, *Electrochem. Solid-State Lett.*, 2011, **14**, F5–F8.
27 Q. H. Zhang, W. D. Han, Y. J. Hong and J. G. Yu, *Catal. Today*, 2009, **148**, 335–340.
28 Q. Fu and T. Wagner, *Surf. Sci. Rep.*, 2007, **62**, 431–498.
29 R. L. Anderson, *Solid-State Electron.*, 1962, **5**, 341–351.
30 I. H. Tseng, W. C. Chang and J. C. S. Wu, *Appl. Catal., B*, 2002, **37**, 37–48.
31 S. C. Roy, O. K. Varghese, M. Paulose and C. A. Grimes, *ACS Nano*, 2010, **4**, 1259–1278.
32 Z. Li, J. Liu, D. Wang, Y. Gao and J. Shen, *Int. J. Hydrogen Energy*, 2012, **37**, 6431–6437.
33 D. Liu, Y. Fernández, O. Ola, S. Mackintosh, M. Maroto-Valer, C. M. A. Parlett, A. F. Lee and J. C. S. Wu, *Catal. Commun.*, 2012, **25**, 78–82.
34 H. Irie, S. Miura, K. Kamiya and K. Hashimoto, *Chem. Phys. Lett.*, 2008, **457**, 202–205.
35 M. Liu, X. Q. Qiu, M. Miyauchi and K. Hashimoto, *Chem. Mater.*, 2011, **23**, 5282–5286.
36 F. Boccuzzi, A. Chiorino, G. Martra, M. Gargano, N. Ravasio and B. Carrozzini, *J. Catal.*, 1997, **165**, 129–139.
37 F. Boccuzzi, A. Chiorino, M. Gargano and N. Ravasio, *J. Catal.*, 1997, **165**, 140–149.
38 Y. Shiraishi, H. Sakamoto, Y. Sugano, S. Ichikawa and T. Hirai, *ACS Nano*, 2013, **7**, 9287–9297.
39 L. Li, Z. Xu, F. Liu, Y. Shao, J. Wang, H. Wan and S. Zheng, *J. Photochem. Photobiol., A*, 2010, **212**, 113–121.
40 J. Y. Park, H. Lee, J. R. Renzas, Y. Zhang and G. A. Somorjai, *Nano Lett.*, 2008, **8**, 2388–2392.
41 H. Chen, S. Chen, X. Quan, H. Yu, H. Zhao and Y. Zhang, *J. Phys. Chem. C*, 2008, **112**, 9285–9290.
42 G. A. Somorjai, K. M. Bratlie, M. O. Montano and J. Y. Park, *J. Phys. Chem. B*, 2006, **110**, 20014–20022.
43 Y. K. Lee, C. H. Jung, J. Park, H. Seo, G. A. Somorjai and J. Y. Park, *Nano Lett.*, 2011, **11**, 4251–4255.
44 M. W. Knight, Y. Wang, A. S. Urban, A. Sobhani, B. Y. Zheng, P. Nordlander and N. J. Halas, *Nano Lett.*, 2013, **13**, 1687–1692.
45 C. Clavero, *Nat. Photonics*, 2014, **8**, 95–103.
46 J. S. DuChene, B. C. Sweeny, A. C. Johnston-Peck, D. Su, E. A. Stach and W. D. Wei, *Angew. Chem., Int. Ed.*, 2014, **53**, 7887–7891.
47 X. Ma, Y. Dai, L. Yu and B. Huang, *ACS Appl. Mater. Interfaces*, 2014, **6**, 12388–12394.
48 J. Y. Park, S. M. Kim, H. Lee and B. Naik, *Catal. Lett.*, 2014, **144**, 1996–2004.
49 L. J. Brennan, F. Purcell-Milton, A. S. Salmeron, H. Zhang, A. O. Govorov, A. V. Fedorov and Y. K. Gun'ko, *Nanoscale Res. Lett.*, 2015, **10**, 1–12.

50 M. Anpo, *Catal. Surv. Asia*, 1997, **1**, 169–179.
51 H. Yoo, C. Bae, Y. Yang, S. Lee, M. Kim, H. Kim, Y. Kim and H. Shin, *Nano Lett.*, 2014, **14**, 4413–4417.
52 L. Gomathi Devi and S. Girish Kumar, *Cent. Eur. J. Chem.*, 2011, **9**, 959–961.
53 J. Kim, J. Lee and W. Choi, *Chem. Commun.*, 2008, 756–758.
54 S. K. Parayil, H. S. Kibombo, C.-M. Wu, R. Peng, T. Kindle, S. Mishra, S. P. Ahrenkiel, J. Baltrusaitis, N. M. Dimitrijevic, T. Rajh and R. T. Koodali, *J. Phys. Chem. C*, 2013, **117**, 16850–16862.
55 J. Zhang, M. Li, Z. Feng, J. Chen and C. Li, *J. Phys. Chem. B*, 2005, **110**, 927–935.
56 G. Wang, H. Wang, Y. Ling, Y. Tang, X. Yang, R. C. Fitzmorris, C. Wang, J. Z. Zhang and Y. Li, *Nano Lett.*, 2011, **11**, 3026–3033.
57 W. Eberhardt, P. Fayet, D. M. Cox, Z. Fu, A. Kaldor, R. Sherwood and D. Sondericker, *Phys. Rev. Lett.*, 1990, **64**, 780–783.
58 M. H. Park, J. H. Li, A. Kumar, G. Li and Y. Yang, *Adv. Funct. Mater.*, 2009, **19**, 1241–1246.
59 K. M. Coakley, Y. Liu, C. Goh and M. D. McGehee, *MRS Bull.*, 2005, **30**, 37–40.
60 W. Mönch, *J. Appl. Phys.*, 2010, **107**, 013706.
61 B. Henrist, N. Hilleret, C. Scheuerlein and M. Taborelli, *Appl. Surf. Sci.*, 2001, **172**, 95–102.
62 J. Chen, E. Louis, J. Verhoeven, R. Harmsen, C. J. Lee, M. Lubomska, M. van Kampen, W. van Schaik and F. Bijkerk, *Appl. Surf. Sci.*, 2010, **257**, 354–361.
63 C. Ruiz, R. G. González Huerta, M. A. Valenzuela and N. Alonso-Vante, *Top. Catal.*, 2011, **54**, 512–518.
64 O. K. Varghese, M. Paulose, T. J. LaTempa and C. A. Grimes, *Nano Lett.*, 2009, **9**, 731–737.
65 W.-J. Lee, M. Alhosan, S. L. Yohe, N. L. Macy and W. H. Smyrl, *J. Electrochem. Soc.*, 2008, **155**, B915–B920.
66 S. H. Kang, Y.-E. Sung and W. H. Smyrl, *J. Electrochem. Soc.*, 2008, **155**, B1128–B1135.
67 D. C. Gleason-Rohrer, B. S. Brunschwig and N. S. Lewis, *J. Phys. Chem. C*, 2013, **117**, 18031–18042.
68 T. C. Leung, C. L. Kao, W. S. Su, Y. J. Feng and C. T. Chan, *Phys. Rev. B: Condens. Matter Mater. Phys.*, 2003, **68**, 195408.
69 P. Pu, H. Cachet, E. Ngaboyamahina and E. M. M. Sutter, *J. Solid State Electrochem.*, 2013, **17**, 817–828.
70 P. Kar, A. Mohammadpour, B. D. Wiltshire, A. M. Askar and K. Shankar, *Curr. Nanosci.*, 2015, **11**, 593–614.
71 S. Kurian, H. Seo and H. Jeon, *J. Phys. Chem. C*, 2013, **117**, 16811–16819.
72 H.-K. Lyeo, A. A. Khajetoorians, L. Shi, K. P. Pipe, R. J. Ram, A. Shakouri and C. K. Shih, *Science*, 2004, **303**, 816–818.
73 S. Kim, S.-J. Hwang and W. Choi, *J. Phys. Chem. B*, 2005, **109**, 24260–24267.
74 J. Lee and W. Choi, *J. Phys. Chem. B*, 2005, **109**, 7399–7406.
75 W. Choi, *Catal. Surv. Asia*, 2006, **10**, 16–28.
76 H. Park, J. Lee and W. Choi, *Catal. Today*, 2006, **111**, 259–265.
77 J. Kim, D. Monllor-Satoca and W. Choi, *Energy Environ. Sci.*, 2012, **5**, 7647–7656.
78 V. P. Zhdanov and B. Kasemo, *Surf. Sci.*, 1999, **432**, L599–L603.
79 P. Sangpour, F. Hashemi and A. Z. Moshfegh, *J. Phys. Chem. C*, 2010, **114**, 13955–13961.
80 W. Zhao, C. Chen, X. Li, J. Zhao, H. Hidaka and N. Serpone, *J. Phys. Chem. B*, 2002, **106**, 5022–5028.